

Manipulating Interfacial Nanostructure to Achieve High-Performance All-Solid-State Lithium-Ion Batteries

Changhong Wang, Xia Li, Yang Zhao, Mohammad N. Banis, Jianwen Liang, Xiaona Li, Yipeng Sun, Keegan R. Adair, Qian Sun, Yulong Liu, Feipeng Zhao, Sixu Deng, Xiaoting Lin, Ruying Li, Yongfeng Hu, Tsun-Kong Sham, Huan Huang, Li Zhang, Rong Yang, Shigang Lu, and Xueliang Sun*

All-solid-state lithium-ion batteries (ASSLIBs) have gained substantial attention worldwide due to their intrinsic safety and high energy density. However, the large interfacial resistance of ASSLIBs, which originates from the interfacial reactions and inferior electrode–electrolyte contact between electrodes and solid electrolytes, dramatically constrains their electrochemical performance. Here a dual shell interfacial nanostructure is rationally designed to enable high-performance ASSLIBs, in which the inner shell LiNbO_3 suppresses the interfacial reactions while the outer shell $\text{Li}_{10}\text{GeP}_2\text{S}_{12}$ enables intimate electrode–electrolyte contact. As a result, the dual shell structured $\text{Li}_{10}\text{GeP}_2\text{S}_{12}@\text{LiNbO}_3@\text{LiCoO}_2$ exhibits a high initial specific capacity of 125.8 mAh g^{-1} (1.35 mAh cm^{-2}) with an initial Coulombic efficiency of 90.4% at 0.1 C and 87.7 mAh g^{-1} at 1 C. More importantly, in situ X-ray absorption near edge spectroscopy was performed for the first time to reveal the interfacial reactions between $\text{Li}_{10}\text{GeP}_2\text{S}_{12}$ and LiCoO_2 . This dual shell nanostructure demonstrates an ideal interfacial configuration for realizing high-performance ASSLIBs.

1. Introduction

Safe and high-energy-density rechargeable lithium-ion batteries are in great demand for large-scale energy storage systems and long-range electric vehicles. Conventional lithium-ion batteries (LIBs), which employ organic liquid electrolytes (LEs), have difficulty in achieving the desired safety standards due to the flammable nature of the organic LEs. Additionally, the limited electrochemical window of the organic LEs restricts the further improvement of the energy density of conventional LIBs,^[1] especially when coupled with high-voltage cathodes and lithium metal anodes. Under intensive investigation for over two decades, all-solid-state lithium ion batteries (ASSLIBs) are now regarded as one of the most promising energy storage systems because of their superior safety and great

potential to meet the target of high energy density.^[2] As an indispensable component of the ASSLIBs, solid-state electrolytes with high ionic conductivity and wide electrochemical windows are indispensable. Over the past years, significant advances have been made in solid-state electrolytes, such as oxide electrolytes,^[2b,3] polymer electrolytes,^[4] and sulfide electrolytes (SEs).^[5] Among them, SEs possess high ionic conductivity (10^{-3} to $10^{-2} \text{ S cm}^{-1}$), particularly $\text{Li}_{9.54}\text{Si}_{1.74}\text{P}_{1.44}\text{S}_{11.7}\text{Cl}_{0.3}$ (25 mS cm^{-1}),^[2a] $\text{Li}_7\text{P}_3\text{S}_{11}$ (17 mS cm^{-1}), $\text{Li}_{10}\text{GeP}_2\text{S}_{12}$ (LGPS) (12 mS cm^{-1}),^[6] and $\text{Li}_{10.35}[\text{Sn}_{0.27}\text{Si}_{1.08}]\text{P}_{1.65}\text{S}_{12}$ (11 S cm^{-1})^[5a] possess ionic conductivities rivaling that of liquid electrolytes (10.2 mS cm^{-1}).^[1] However, the electrochemical performance of SE-based ASSLIBs is constrained by the large interfacial resistance, which is originated from the interfacial reactions and lithium deficient space-charge layer as well as the inferior solid–solid contact between electrode materials and SEs.^[2d,7] With tremendous efforts, various strategies have been proposed to suppress the interfacial resistance, including i) developing interfacial layers (LiNbO_3 (LNO) and $\text{Li}_4\text{Ti}_5\text{O}_{12}$) to suppress the interfacial reactions,^[8] ii) synthesizing soluble solid electrolytes to improve the interfacial contact between electrode materials and SEs,^[9] iii) designing homogeneous and compatible interface,^[10] and iv) using novel

C. Wang, Dr. X. Li, Dr. Y. Zhao, Dr. M. N. Banis, Dr. J. Liang, Dr. X. Li, Y. Sun, K. R. Adair, Dr. Q. Sun, Dr. Y. Liu, F. Zhao, Dr. S. Deng, X. Lin, R. Li, Prof. X. Sun


Department of Mechanical and Materials Engineering
University of Western Ontario
1151 Richmond St, London, ON N6A 3K7, Canada
E-mail: xsun9@uwo.ca

Dr. Y. Hu
Canadian Light Source
44 Innovation Boulevard, Saskatoon, SK S7N 2V3, Canada

Prof. T.-K. Sham
Department of Chemistry
University of Western Ontario
ON N6A 5B9, London, Canada

Dr. H. Huang
Glabat Solid-State Battery Inc.
700 Collip Circle, London, ON N6G 4X8, Canada

Dr. L. Zhang, Dr. R. Yang, Dr. S. Lu
China Automotive Battery Research Institute Co., Ltd.
5th Floor, No. 43, Mining Building
North Sanhuan, Middle Road
Haidian District, Beijing P.C. 100088, China

 The ORCID identification number(s) for the author(s) of this article can be found under <https://doi.org/10.1002/smt.201900261>.

DOI: 10.1002/smt.201900261

solid electrolytes.^[11] However, the electrochemical performance of ASSLIBs is still far behind the standard for practical application.

Inspired by the pioneering success in addressing the challenges of silicon anodes,^[12] sulfur cathodes,^[13] and Li metal anodes^[14] via rational nanostructure design, here we rationally designed a dual shell interfacial nanostructure to enable high-performance ASSLIBs. The inner shell is devised to suppress the interfacial reactions and lithium-deficient space-charge layer (SCL) between electrode materials and SEs. The outer shell is constructed to ensure the intimate solid–solid contact between electrode materials and SEs. As a result, the dual shell structured LGPS@LNO@LCO cathode exhibits a high initial specific capacity of 125.8 mAh g^{−1} (1.35 mAh cm^{−2}) with an initial coulombic efficiency of 90.4% at 0.1 C and 87.7 mAh g^{−1} at 1 C. Moreover, the charge and discharge curves of the dual shell structured LGPS@LNO@LCO exactly match those in liquid electrolytes, suggesting the negligible polarization and complete utilization of LCO in ASSLIBs. Additionally, in-situ XANES was performed to reveal the interfacial reactions between LCO and LGPS for the first time. This demonstration shed light on the interfacial nanostructure design to achieve high-performance SE-based ASSLIBs.

2. Results and Discussion

As a proof-of-concept study, the typical active material LiCoO₂ (LCO), the most well-known solid-state sulfide electrolyte Li₁₀GeP₂S₁₂, and the high ionically conductive interfacial layer LiNbO₃ are chosen, although the concept is not limited to these materials. In general, when directly mixing LCO with LGPS without any interfacial coating, a highly resistive layer will form at the interface between LCO and LGPS during the initial charge process, which intrinsically blocks the Li⁺ transfer.^[8a] Furthermore, a lithium-deficient space-charge layer will form at the interface,^[15] under this scenario, ASSLIBs can be barely charged due to the significant interfacial resistance in the ASSLIBs (Figure 1A). With one shell (LNO) isolating the direct contact between LCO and LGPS, the interfacial reactions and lithium-deficient SCL can be suppressed.^[16] Atomic layer deposition is employed to conformally construct the inner layer LNO.^[2d,17] In this case, ASSLIBs can be operated at low current, because the interfacial Li⁺ flux is limited by insufficient ionic contact between LCO and LGPS (Figure 1B). In addition, the aggregation of LCO and LGPS particles could lead to the incomplete utilization and serious polarization of LCO in ASSLIBs.^[18] The remedy to this case is to construct a dual shell interfacial configuration. As shown in Figure 1C, when LGPS with a high ionic conductivity

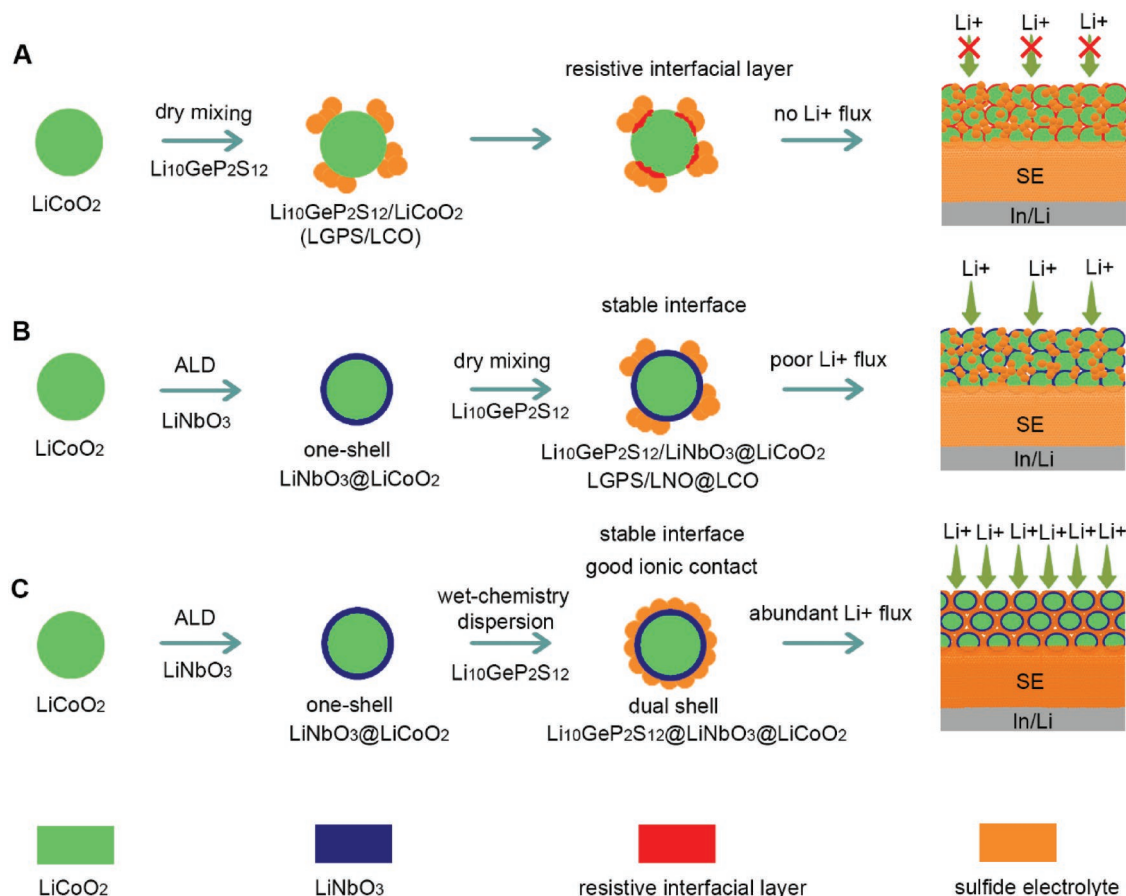


Figure 1. Schematic diagram of ASSLIBs with various interfacial nanostructure. A) LiCoO₂ directly mixed with Li₁₀GeP₂S₁₂ without interfacial design for ASSLIBs. B) A one-shell LiNbO₃@LiCoO₂ cathode for ASSLIBs. C) A dual shell LGPS@LNO@LCO for ASSLIBs.

is further dispersed on the one-shell LNO@LCO particle via a wet-chemistry dispersion process, intimate solid-solid contact between LGPS and LNO@LCO can be achieved, thus enabling an abundant Li^+ flux across the interface. It should be mentioned that the dispersion process is different from the previous soluble sulfide electrolyte coating, in which a post-annealing process is required to crystallize SEs.^[9a,b] In addition, the wet-chemistry dispersion process can be easily developed with other SEs without the post-annealing process. The detailed experimental procedure can be found in the Supporting Information.

The particle size of the pristine commercial LCO was found to be around 6–15 μm by scanning electron microscopy (SEM) (Figure S1, Supporting Information). 5 nm LNO was uniformly and conformably coated on the LCO surface by atomic layer deposition (ALD), as confirmed by the transmission electron microscopy (TEM) images in Figure 2A,B. The energy dispersive X-ray spectroscopic (EDX) mapping of Co, Nb, and O

were detected by high-angle annular dark-field scanning transmission electron microscopy (HAADF-STEM) (Figure 2C), explicitly confirming the uniform coating of LNO on the LCO surface. It should be mentioned that the interfacial coating in previous works is mainly realized by the sol-gel method,^[8,19] which cannot guarantee the uniformity and conformality of ALD coatings.^[20] Figure 2D shows an SEM image of LNO@LCO/LGPS composite synthesized by conventional dry mixing, which clearly shows the aggregation of LCO and LGPS particles and inferior solid-solid contact between LNO@LCO and LGPS. Compared to the LNO@LCO/LGPS composites, the uniform coverage of LGPS on LNO@LCO particles can be seen in the LGPS@LNO@LCO composites (Figure 2E), implying the dual shell structure was successfully realized by the wet-chemistry dispersion process. Furthermore, the cross-section image of LGPS@LNO@LCO composites milled by focused ion beam (FIB) is presented in Figure 2F. In addition, the corresponding

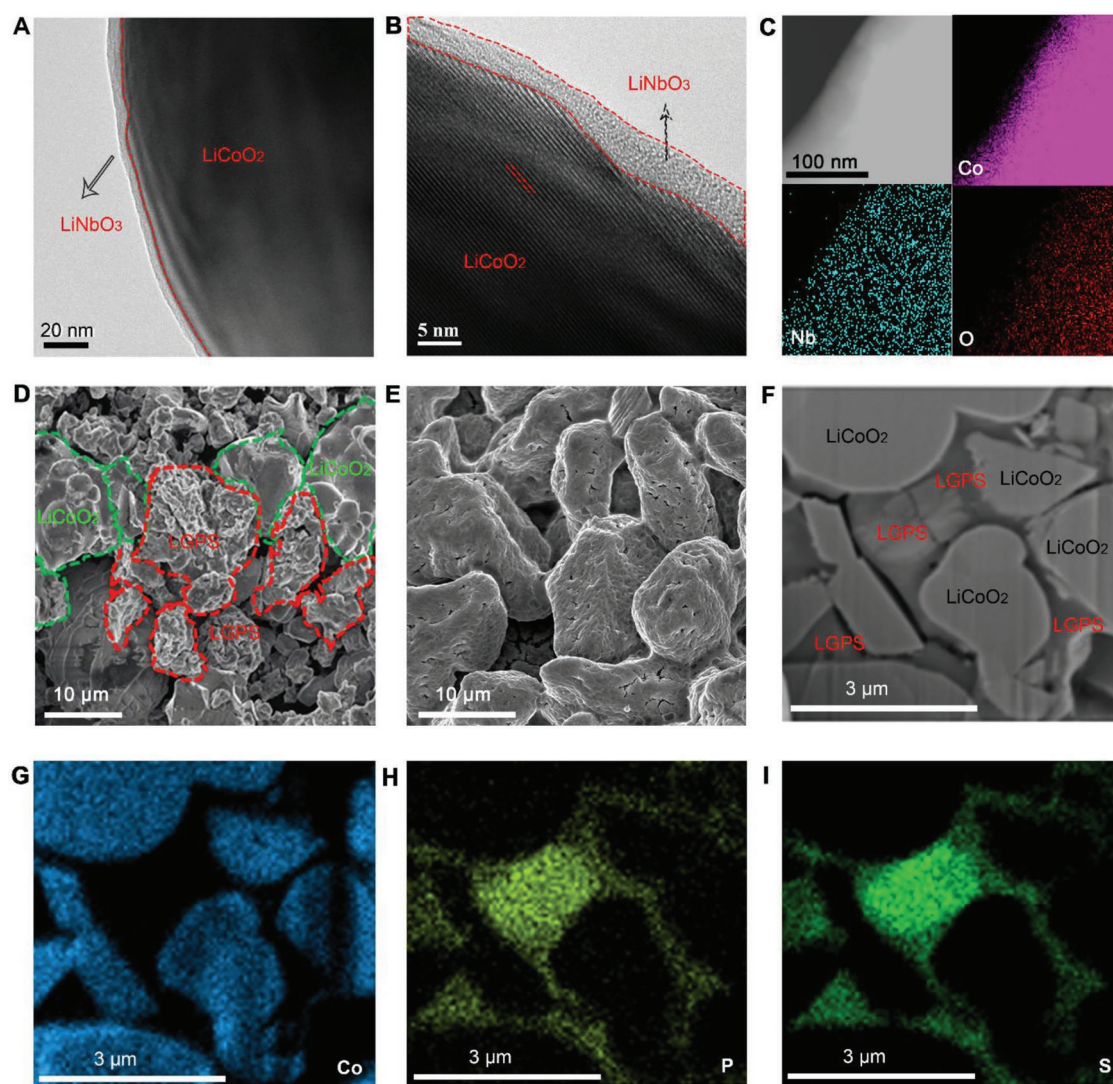


Figure 2. Structural and elemental analysis of one-shell LNO@LCO and dual shell LGPS@LNO@LCO. A) A TEM image of one-shell LNO@LCO particles. B) A high-resolution TEM image of one-shell LNO@LCO particles. C) Energy dispersive X-ray spectroscopic (EDS) mapping of Co, Nb, and O by HAADF-STEM. D) SEM image of the one-shell LNO@LCO/LGPS electrode. E) SEM image of the mixture of the dual shell structured LGPS@LNO@LCO electrode. F) FIB cross-section image of LGPS@LNO@LCO. G) Co mapping. H) P mapping. I) S mapping.

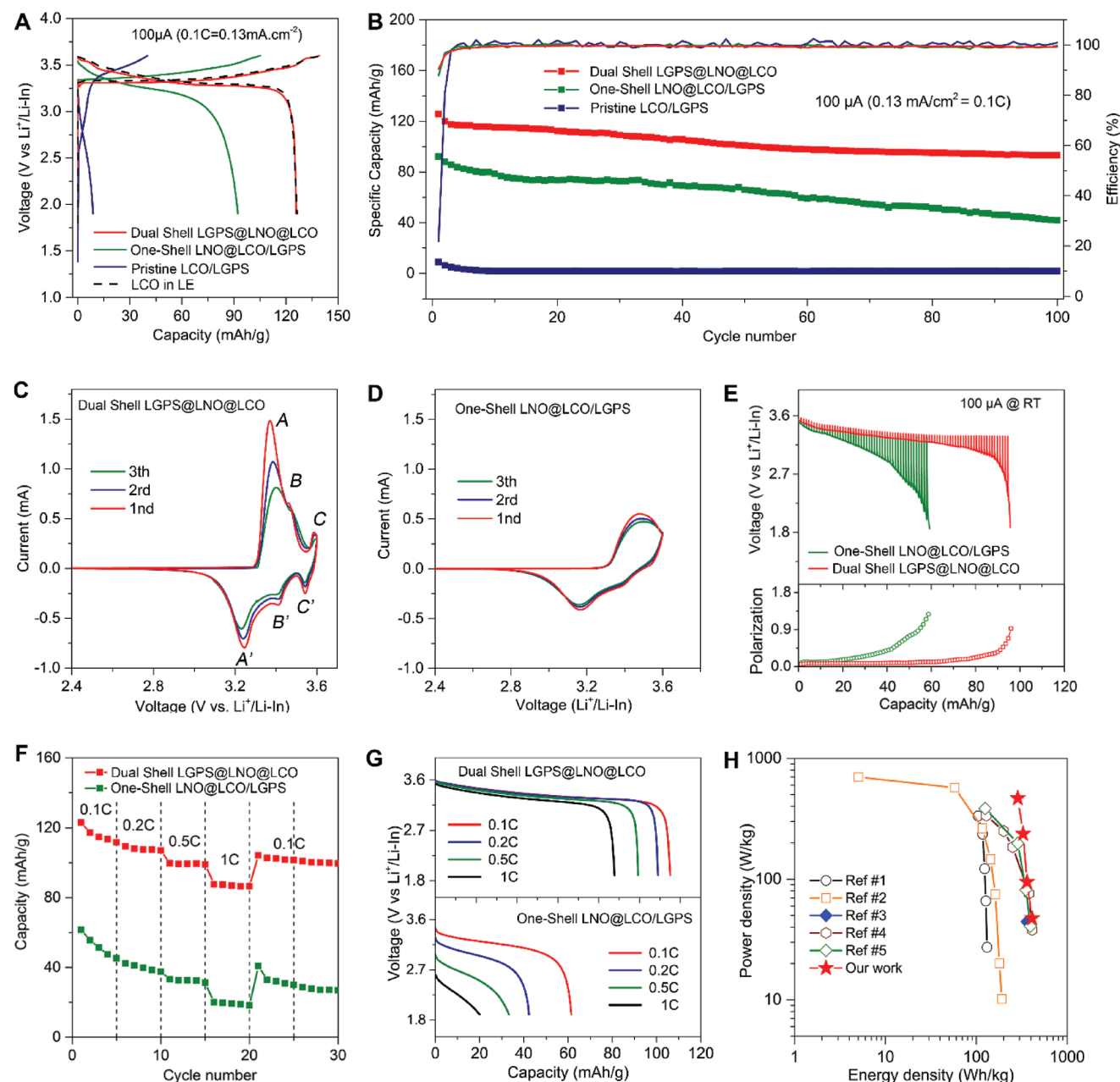


Figure 3. Electrochemical performance of ASSLIBs with pristine LCO, one-shell LNO@LCO, and dual-shell structured LGPS@LNO@LCO. A) Charge-discharge curves. B) Cycling stability and coulombic efficiency. C) CV curves of dual shell structured LGPS@LNO@LCO. D) CV curves of one-shell LNO@LCO/LGPS electrodes. E) Galvanostatic Intermittent Titration Technique (GITT). F) Rate performance. G) Discharge curves at various current densities. H) Ragone plot.

EDX mapping of Co, P, and S are shown in Figures 2G,H,I, respectively, further confirming that the outer LGPS layer is uniformly and conformally coated on LNO@LCO surfaces. Further EDX mapping images (including Ge mapping and Nb mapping) of LGPS@LNO@LCO can be found in Figure S2 (Supporting Information), which also confirms the LNO shell on the LCO surface. To be the best of our knowledge, this is the first time to demonstrate the LGPS coating on the electrode materials via a wet-chemistry dispersion process.

The electrochemical performances of ASSLIBs with various interfacial structures were evaluated thoroughly. **Figure 3A** exhibits the typical charge-discharge curves of pristine LCO, one-shell LNO@LCO, dual shell structured LGPS@LNO@LCO, and LCO in liquid electrolytes (LE), respectively. The pristine LCO exhibits an initial charge capacity of 40.1 mAh g^{-1} and discharge capacity of 8.8 mAh g^{-1} at 0.1 C ($1 \text{ C} = 1.3 \text{ mA cm}^{-2} = 140 \text{ mA g}^{-1}$). The initial coulombic efficiency is only 21.9%. The low coulombic efficiency and significant polarization indicate serious interfacial reactions during

the initial charging process. In addition, the slope at the very beginning of the charge curve is an indicator of a lithium-deficient SCL between LCO and LGPS.^[15,21] The one-shell LNO@LCO exhibits an initial discharge capacity of 92.2 mAh g⁻¹ with the coulombic efficiency of 89.1%. Interestingly, the slope before Li⁺ delithiation is totally disappeared, suggesting that the one-shell LNO@LCO can suppress the interfacial reactions and SCL between LCO and LGPS. However, the polarization between charge and discharge curves is still obvious, which is caused by the poor ionic contact between LNO@LCO and LGPS. The dual shell structured LGPS@LNO@LCO presents an initial capacity of 125.8 mAh g⁻¹ with an initial coulombic efficiency of 90.4%. It is worthwhile to mention that the charge-discharge curves of the dual shell LGPS@LNO@LCO exactly match those of LCO in liquid electrolytes under the same current density (Figure S3, Supporting Information), demonstrating that the dual shell structured LGPS@LNO@LCO can achieve the full utilization of LCO with a negligible polarization in ASSLIBs. The electrochemical impedance spectroscopy (EIS) was performed to analyze the interfacial resistance of pristine LCO, one-shell LNO@LCO, and dual shell structured LGPS@LNO@LCO after the initial charge process (Figure S4, Supporting Information). The interfacial resistance of the pristine LCO after the first charge process is over 3000 ohms, which is reduced to 150 ohms with LNO inner shell protection, and further reduced to 68 ohms when LGPS is coated on the LNO@LCO particles. The reduction in resistance suggests that the inner shell LNO can suppress the interfacial reactions and the outer shell LGPS can improve the interfacial contact between LNO@LCO and LGPS.

Figure 3B shows the cycle stability of pristine LCO, one-shell LNO@LCO, and dual shell structured LGPS@LNO@LCO and the corresponding coulombic efficiencies (Figure S5, Supporting Information). Pristine LCO shows no capacity after several cycles, which is due to the serious interfacial reactions between pristine LCO and LGPS. Comparatively, the one-shell LNO@LCO shows higher capacity and longer cycle stability. However, the capacity decays rapidly and is still far behind theoretical capacity of LCO. The reason was believed to be the detachment of LCO from LGPS induced by the volume change upon cycling (Figure S6, Supporting Information). The dual shell structured LGPS@LNO@LCO shows a higher capacity of 125.8 mAh g⁻¹, which can still retain a capacity of 90.3 mAh g⁻¹ after 100 cycles. Figure 3C presents the cyclic voltammogram (CV) profiles of the dual shell structured LGPS@LNO@LCO and one-shell LNO@LCO, respectively. The three pairs of redox peaks of LGPS@LNO@LCO can be clearly seen. The A–A' redox peaks are related to the insulator–metal transition with the coexistence of two distinct hexagonal phases.^[19,22] The B–B', and C–C' redox peaks are associated with the phase transition from the hexagonal structure (O3) to the monoclinic structure of LCO.^[22] Comparatively, the CV of LNO@LCO shows obvious polarization and smaller peak currents (Figure 3D), suggesting the limited Li⁺ flux across the interface between LCO and LGPS. The Galvanostatic Intermittent Titration Technique (GITT) was further utilized to analyze the polarization and lithium ion (Li⁺) diffusion efficiency of LNO@LCO and LGPS@LNO@LCO. Figure 3E shows the GITT curves and polarization curves of LNO@LCO and LGPS@LNO@LCO. Obviously,

the polarization of LGPS@LNO@LCO is smaller than that of LNO@LCO. Based on the GITT theoretical analysis, the Li⁺ diffusion efficiency of the dual shell LGPS@LNO@LCO electrode is almost 4 orders of magnitude higher than that of one-shell LNO@LCO electrodes (Figure S7 and Table S1, Supporting Information), indicating that the contact area between LNO@LCO and LGPS is dramatically enhanced by designing dual shell interfacial structure.

When tested at various current densities, the one-shell LNO@LCO shows limited capacity and large polarization at a high current density (Figure 3F). Specifically, one-shell LNO@LCO exhibit a specific capacity of 20.0 mAh g⁻¹ with a large polarization at 1 C, while the dual shell structured LGPS@LNO@LCO presents a capacity of 87.7 mAh g⁻¹ with a negligible polarization at 1 C (Figure 3G). The reason behind the increased capacity and negligible polarization could be due to the high ionic conductivity (1.2×10^{-3} S cm⁻¹, Figure S8, Supporting Information) of the outer shell LGPS. Figure 3H compares the electrochemical performance with all previously reported results in the Ragone plot. The sources of the data are listed in Table S2 (Supporting Information). It is apparent that the electrochemical performance of the dual shell structured LGPS@LNO@LCO overtakes previous results, especially the power density.^[6a,8a,21]

To unveil the interfacial reactions between LCO and LGPS and functionality of the inner shell LNO, in situ X-ray absorption near edge spectroscopy (XANES) was performed. Figure 4A,C present the in-operando sulfur K-edge XANES and the discharge-charge profiles of pristine LCO and one-shell LNO@LCO, respectively. The electrochemical phenomena are completely consistent with the results in Figure 3A. Comparing the S K-edge XANES, the edge jump of the LGPS before the electrochemical reaction is at 2470 eV, which is corresponding to the one level excitation of an electron from the K shell.^[23] Due to the weak signal to noise ratio, the first-order derivation spectra was subtracted in Figure 4B,D. Pristine LCO/LGPS presents a lot of shoulder peaks at 2470 eV (red bar) and 2472 eV (green bar) during the charge-discharge process, while LNO@LCO/LGPS does not, implying that the inner shell LNO can suppress the interfacial reactions between LCO and LGPS. However, the changes on other elements are not clarified, such as phosphorus and germanium. As a remedy, surface-sensitive X-ray photoelectron spectroscopy (XPS) was performed to further examine the chemical information on P, Ge, and S.

Figure 5 shows the ex situ XPS results of S 2p, P 2p, and Ge 3d from pristine LGPS, bare LCO/LGPS after 100 cycles, and one-shell LNO@LCO/LGPS after 100 cycles, respectively. Assignment of each peak can be found in Table S3 (Supporting Information). In S 2p spectra (Figure 5A), S of LGPS is highly oxidized to –S–S– or CoS_x in comparison with S spectra of pristine LGPS. In addition, sulfite and sulfate species were also detected, which is also caused by the oxidation of LGPS by LCO during the charge-discharge process.^[19,21] Interestingly, the intensity of oxidation peaks is reduced with the inner LNO shell (Figure 5A, bottom), suggesting the inner shell LNO can alleviate the oxidation of LCO during the charge-discharge process. Figure 5B shows the comparison of P 2p spectra. P 2p spectra of bare LCO/LGPS exhibit more intensive P₂S₆²⁻ peaks, suggesting P of bare LCO/LGPS is highly oxidized after cycling,

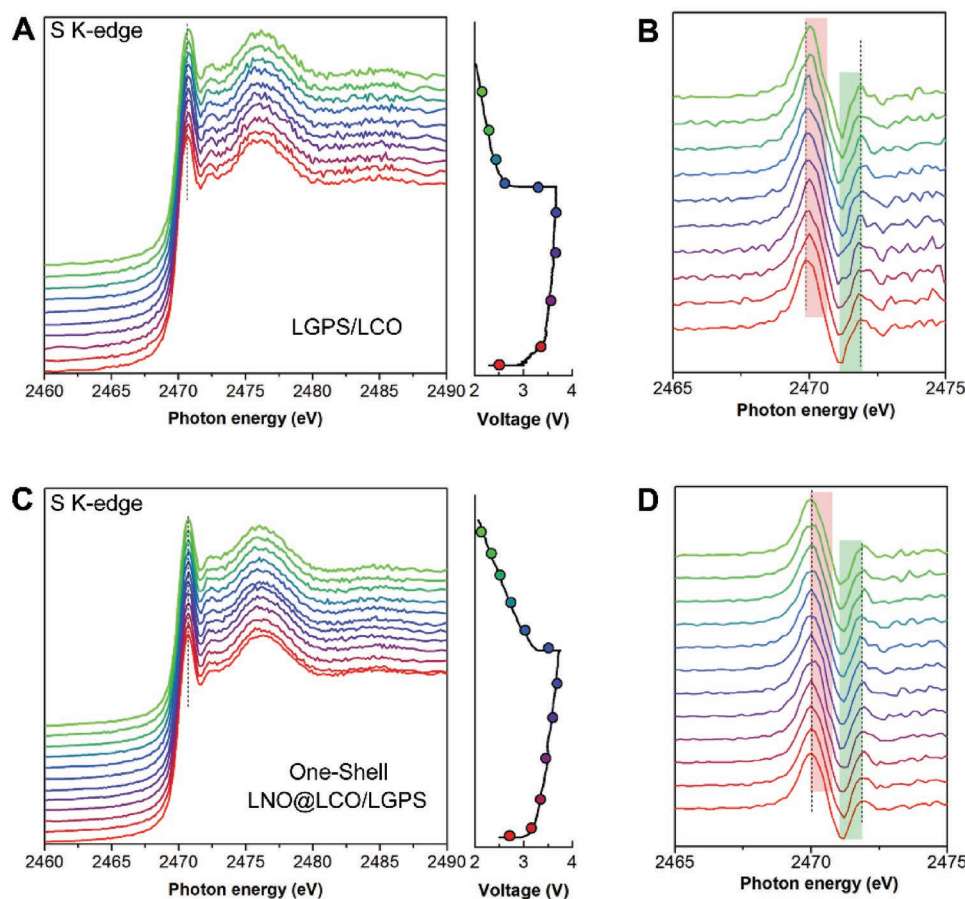


Figure 4. In situ XANES of ASSLIBs during the initial charge–discharge process. A) S K-edge of the bare LCO/LGPS cathode. B) The first deviation of the S K-edge spectra of the bare LCO/LGPS electrode. C) S K-edge of the one-shell LNO@LCO/LGPS electrode. D) The first deviation of S K-edge spectra of one-shell LNO@LCO/LGPS electrodes.

In LNO@LCO/LGPS samples, the intensity of $\text{P}_2\text{S}_6^{2-}$ peaks is strongly suppressed by the inner shell LNO protection. Similarly, in terms of Ge 3d spectra (Figure 5C), the intensity associated with the oxidized species, such as GeS_x and/or GeO_2 , is reduced in the one-shell LNO@LCO samples, implying that the oxidation of Ge of LGPS is also suppressed by the inner shell LNO. All the results explicitly demonstrate that the inner shell can inhibit the oxidation reactions of LGPS but cannot completely suppress the interfacial oxidation reactions due to the intrinsically narrow electrochemical windows of LGPS.^[24]

To check the internal microstructure of one-shell LNO@LCO and dual shell LGPS@LNO@LCO, the cross-section of electrodes was examined by SEM. The LNO@LCO electrodes show a lot of pores between LGPS and LNO@LCO, which suggests the contact between LNO@LCO and LGPS is inferior (point-to-point contact, Figure 6A–C), limiting the Li^+ flux across the interface. As a sharp contrast, the dual shell structured LGPS@LNO@LCO shows favorable contact between LCO and LGPS. All the LNO@LCO particles are well dispersed in the LGPS matrix (Figure 6D–F), thus providing abundant Li^+ flux across the interface and guaranteeing the high utilization of LCO. Resultantly, the initial charge–discharge curves, active material utilization, and coulombic efficiency of dual shell structured LGPS@LNO@LCO exactly match those of LCO operated in

LEs. All these results confirm that the dual shell interface could overcome the large interfacial resistance originated from the interfacial reactions and inferior interparticle contact between electrode materials and SEs in ASSLIBs.

3. Conclusions

In summary, we rationally designed a dual shell structured LGPS@LNO@LCO for high-performance SE-based ASSLIBs, in which the inner shell LiNbO_3 suppresses the interfacial reactions while the outer shell $\text{Li}_{10}\text{GeP}_2\text{S}_{12}$ enables intimate electrode–electrolyte contact. The interfacial reactions between LGPS and LCO characterized by the in situ XANES and ex situ XPS highlight the necessity of inner shell LNO. The outer shell LGPS coating realized by a universal wet-chemistry dispersion process enables the full utilization and negligible polarization of LCO in SE-based ASSLIBs. As a result, the dual shell structured LGPS@LNO@LCO exhibits a high initial specific capacity of 125.8 mAh g^{-1} (1.35 mAh cm^{-2}) with an initial coulombic efficiency of 90.4% at 0.1 C and 87.7 mAh g^{-1} at 1 C. This dual shell nanostructure demonstrates an ideal interfacial configuration for achieving SE-based ASSLIBs with high-energy density and high-power density.

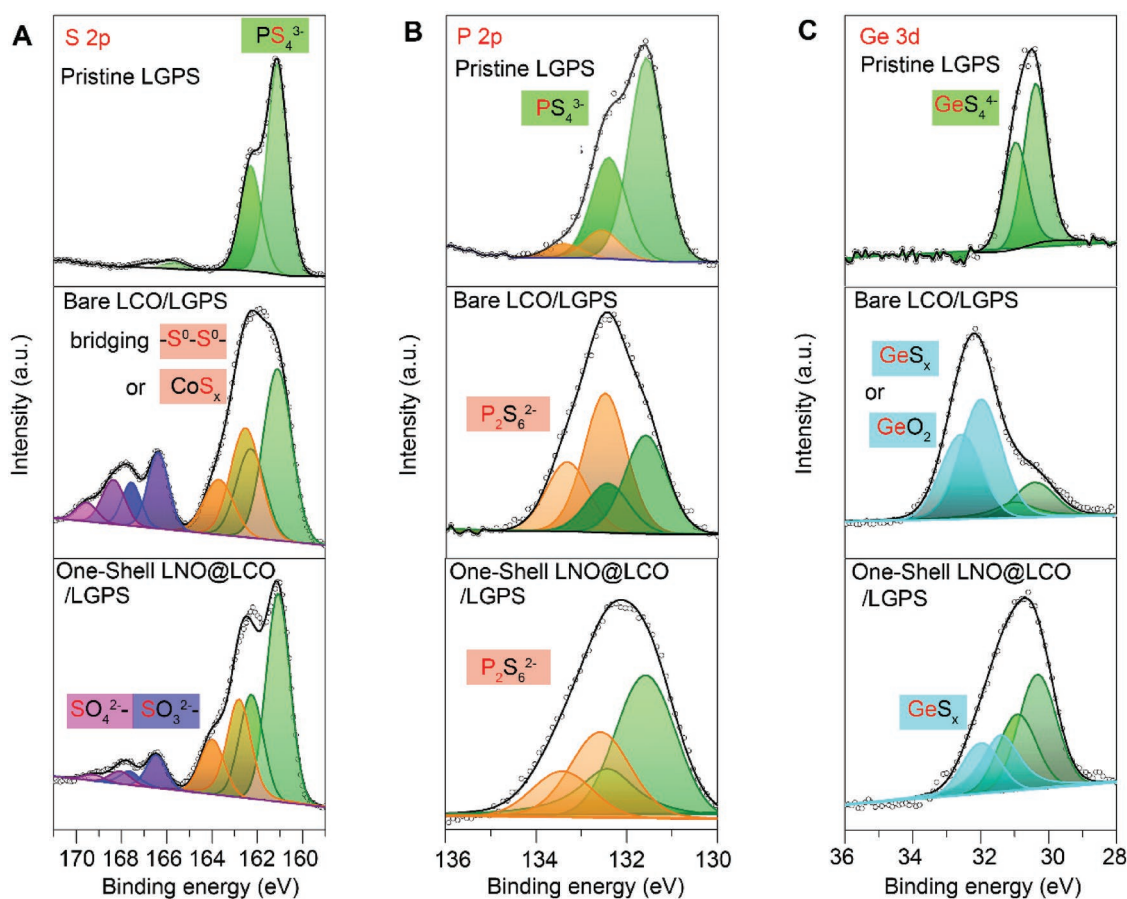


Figure 5. Ex situ XPS characterizations on the pristine LGPS (top), bare LCO/LGPS electrodes after 100 cycles (middle), and one-shell LNO@LCO/LGPS electrodes after 100 cycles (bottom). A) S 2p spectra, B) P 2p spectra, and C) Ge 3d spectra.

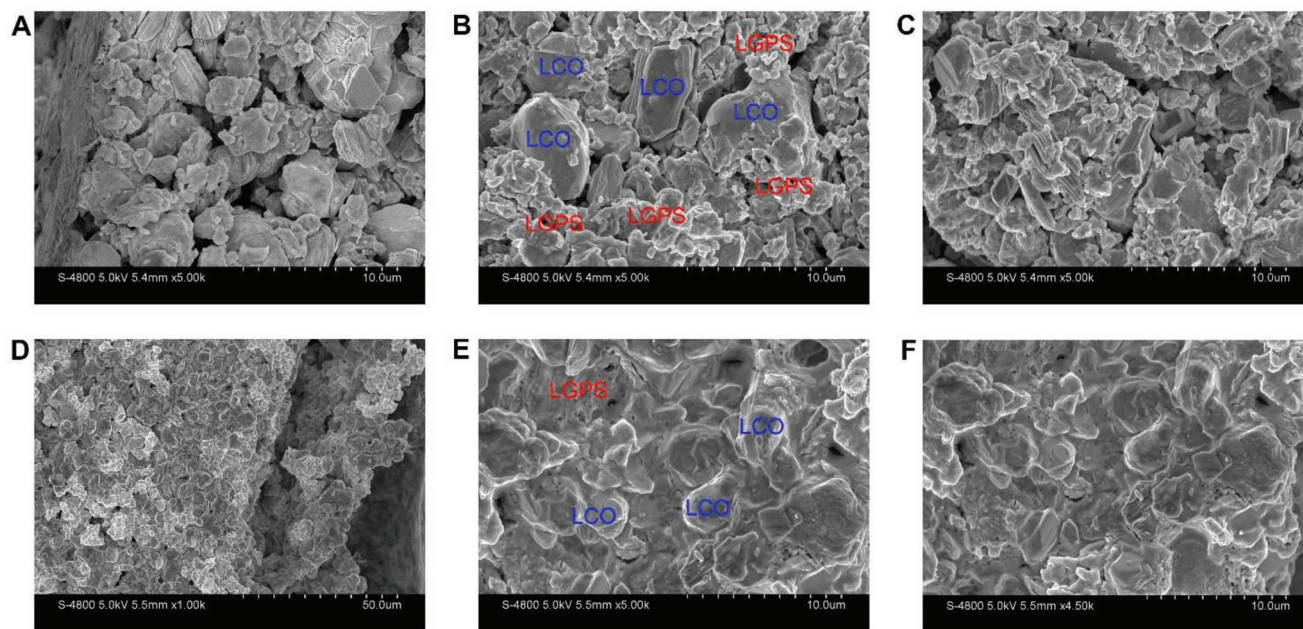


Figure 6. SEM images of cross-section. A–C) one-shell LNO@LCO/LGPS electrodes. D–F) dual shell structured LGPS@LNO@LCO electrodes.

Supporting Information

Supporting Information is available from the Wiley Online Library or from the author.

Acknowledgements

C.W. and X.L. contributed equally to this work. This work was supported by Natural Sciences and Engineering Research Council of Canada (NSERC), Canada Research Chair Program (CRC), Canada Foundation for Innovation (CFI), Ontario Research Fund (ORF), China Automotive Battery Research Institute Co., Ltd., Glabat Solid-State Battery Inc., Canada Light Source (CLS) at University of Saskatchewan, Interdisciplinary Development Initiatives (IDI) by Western University, and University of Western Ontario. X.S. supervised the project. C.W. conceived this idea, synthesized the electrodes, characterized the samples, tested the electrochemical performances, and wrote this manuscript. X.L. and M.B. performed the in situ XAS and TEM characterization in CLS and McMaster University, respectively. X.L. and J.L. helped with experimental optimization. Y.Z. and Y.S. helped with ALD process. K.A. polished the language. R.L. helped with SEM and purchasing all the chemicals. All the authors discussed the results and commented on the manuscript. X.L. thanks the support of Mitacs Elevate Postdoctoral Fellowship. C.W. appreciates the funding support of Mitacs Accelerate Fellowship.

Conflict of Interest

The authors declare no conflict of interest.

Keywords

all-solid-state lithium-ion batteries, interfacial nanostructure design, sulfide electrolytes

Received: April 5, 2019
Published online: April 26, 2019

- [1] K. Xu, *Chem. Rev.* **2004**, *104*, 4303.
- [2] a) Y. Kato, S. Hori, T. Saito, K. Suzuki, M. Hirayama, A. Mitsui, M. Yonemura, H. Iba, R. Kanno, *Nat. Energy* **2016**, *1*, 16030; b) F. Han, J. Yue, C. Chen, N. Zhao, X. Fan, Z. Ma, T. Gao, F. Wang, X. Guo, C. Wang, *Joule* **2018**, *2*, 497; c) J. Janek, W. G. Zeier, *Nat. Energy* **2016**, *1*, 16141; d) Y. Zhao, K. Zheng, X. Sun, *Joule* **2018**, *2*, 2583; e) G. Zhonghui, S. Huabin, F. Lin, Y. Fangliang, Z. Yi, L. Wei, H. Yunhui, *Adv. Mater.* **2018**, *30*, 1705702; f) K. H. Park, Q. Bai, D. H. Kim, D. Y. Oh, Y. Zhu, Y. Mo, Y. S. Jung, *Adv. Energy Mater.* **2018**, *8*, 1800035.
- [3] C. Wang, Q. Sun, Y. Liu, Y. Zhao, X. Li, X. Lin, M. N. Banis, M. Li, W. Li, K. R. Adair, D. Wang, J. Liang, R. Li, L. Zhang, R. Yang, S. Lu, X. Sun, *Nano Energy* **2018**, *48*, 35.
- [4] a) W. Liu, S. W. Lee, D. Lin, F. Shi, S. Wang, A. D. Sendek, Y. Cui, *Nat. Energy* **2017**, *2*, 17035; b) L. Yue, J. Ma, J. Zhang, J. Zhao, S. Dong, Z. Liu, G. Cui, L. Chen, *Energy Storage Mater.* **2016**, *5*, 139.
- [5] a) Y. Sun, K. Suzuki, S. Hori, M. Hirayama, R. Kanno, *Chem. Mater.* **2017**, *29*, 5858; b) S. J. Sedlmaier, S. Indris, C. Dietrich, M. Yavuz, C. Dräger, F. von Seggern, H. Sommer, J. Janek, *Chem. Mater.* **2017**, *29*, 1830; c) C. Wang, Y. Zhao, Q. Sun, X. Li, Y. Liu, J. Liang, X. Li, X. Lin, R. Li, K. R. Adair, L. Zhang, R. Yang, S. Lu, X. Sun, *Nano Energy* **2018**, *53*, 168.
- [6] a) N. Kamaya, K. Homma, Y. Yamakawa, M. Hirayama, R. Kanno, M. Yonemura, T. Kamiyama, Y. Kato, S. Hama, K. Kawamoto, A. Mitsui, *Nat. Mater.* **2011**, *10*, 682; b) S. P. Ong, Y. Mo, W. D. Richards, L. Miara, H. S. Lee, G. Ceder, *Energy Environ. Sci.* **2013**, *6*, 148.
- [7] a) P. K. Ho, B. Qiang, K. D. Hyeon, O. D. Yang, Z. Yizhou, M. Yifei, J. Y. Seok, *Adv. Energy Mater.* **2018**, *8*, 1800035; b) X. Chen, W. He, L.-X. Ding, S. Wang, H. Wang, *Energy Environ. Sci.* **2019**, *12*, 938.
- [8] a) N. Ohta, K. Takada, L. Zhang, R. Ma, M. Osada, T. Sasaki, *Adv. Mater.* **2006**, *18*, 2226; b) N. Ohta, K. Takada, I. Sakaguchi, L. Zhang, R. Ma, K. Fukuda, M. Osada, T. Sasaki, *Electrochem. Commun.* **2007**, *9*, 1486.
- [9] a) D. H. Kim, D. Y. Oh, K. H. Park, Y. E. Choi, Y. J. Nam, H. A. Lee, S.-M. Lee, Y. S. Jung, *Nano Lett.* **2017**, *17*, 3013; b) K. H. Park, D. Y. Oh, Y. E. Choi, Y. J. Nam, L. Han, J.-Y. Kim, H. Xin, F. Lin, S. M. Oh, Y. S. Jung, *Adv. Mater.* **2016**, *28*, 1874; c) A. Banerjee, K. H. Park, J. W. Heo, Y. J. Nam, C. K. Moon, S. M. Oh, S.-T. Hong, Y. S. Jung, *Angew. Chem., Int. Ed.* **2016**, *55*, 9634.
- [10] a) F. D. Han, T. Gao, Y. J. Zhu, K. J. Gaskell, C. S. Wang, *Adv. Mater.* **2015**, *27*, 3473; b) X. Li, J. Liang, X. Li, C. Wang, J. Luo, R. Li, X. Sun, *Energy Environ. Sci.* **2018**, *11*, 2828.
- [11] T. Asano, A. Sakai, S. Ouchi, M. Sakaida, A. Miyazaki, S. Hasegawa, *Adv. Mater.* **2018**, *30*, 1803075.
- [12] C. K. Chan, H. Peng, G. Liu, K. McIlwrath, X. F. Zhang, R. A. Huggins, Y. Cui, *Nat. Nanotechnol.* **2008**, *3*, 31.
- [13] X. L. Ji, K. T. Lee, L. F. Nazar, *Nat. Mater.* **2009**, *8*, 500.
- [14] D. Lin, Y. Liu, Z. Liang, H.-W. Lee, J. Sun, H. Wang, K. Yan, J. Xie, Y. Cui, *Nat. Nanotechnol.* **2016**, *11*, 626.
- [15] K. Takada, N. Ohta, L. Zhang, K. Fukuda, I. Sakaguchi, R. Ma, M. Osada, T. Sasaki, *Solid State Ionics* **2008**, *179*, 1333.
- [16] M. Sumita, Y. Tanaka, M. Ikeda, T. Ohno, *J. Phys. Chem. C* **2016**, *120*, 13332.
- [17] a) B. Wang, Y. Zhao, M. N. Banis, Q. Sun, K. R. Adair, R. Li, T.-K. Sham, X. Sun, *ACS Appl. Mater. Interfaces* **2018**, *10*, 1654; b) Y. Zhao, X. Sun, *ACS Energy Lett.* **2018**, *3*, 899.
- [18] a) K. Suzuki, N. Mashimo, Y. Ikeda, T. Yokoi, M. Hirayama, R. Kanno, *ACS Appl. Energy Mater.* **2018**, *1*, 2373; b) J. Kim, M. Eom, S. Noh, D. Shin, *J. Power Sources* **2013**, *244*, 476.
- [19] W. Zhang, F. H. Richter, S. P. Culver, T. Leichtweiss, J. G. Lozano, C. Dietrich, P. G. Bruce, W. G. Zeier, J. Janek, *ACS Appl. Mater. Interfaces* **2018**, *10*, 22226.
- [20] X. Meng, X.-Q. Yang, X. Sun, *Adv. Mater.* **2012**, *24*, 3589.
- [21] W. Zhang, T. Leichtweiß, S. P. Culver, R. Koerver, D. Das, D. A. Weber, W. G. Zeier, J. Janek, *ACS Appl. Mater. Interfaces* **2017**, *9*, 35888.
- [22] Q. Liu, X. Su, D. Lei, Y. Qin, J. Wen, F. Guo, Y. A. Wu, Y. Rong, R. Kou, X. Xiao, F. Aguesse, J. Bareño, Y. Ren, W. Lu, Y. Li, *Nat. Energy* **2018**, *3*, 936.
- [23] X. Li, M. Banis, A. Lushington, X. Yang, Q. Sun, Y. Zhao, C. Liu, Q. Li, B. Wang, W. Xiao, C. Wang, M. Li, J. Liang, R. Li, Y. Hu, L. Goncharova, H. Zhang, T.-K. Sham, X. Sun, *Nat. Commun.* **2018**, *9*, 4509.
- [24] a) F. D. Han, Y. Z. Zhu, X. F. He, Y. F. Mo, C. S. Wang, *Adv. Energy Mater.* **2016**, *6*, 9; b) F. Wu, W. Fitzhugh, L. Ye, J. Ning, X. Li, *Nat. Commun.* **2018**, *9*, 4037.